# The first GISMO pool: bolometer behaviour

G. Bruni, C. Kramer, N. Billot, G. Quintana-Lacaci

August 3, 2012

*Abstract*

We use data taken with the Goddard-IRAM Superconducting 2mm Observer camera (GISMO) at the 30m telescope during two dedicated weeks of pooled observing projects between April 10th to 24th, 2012, to study some aspects of the performance of GISMO.

For the entire analysis presented here, we used the latest version of the `crush` data processing package 2.12-1. To get an overview, the entire data set taken during 72 hours of on-source time, were processed with a standard pipeline to produce a new logsheet. The distribution of noise equivalent flux densities (NEFD) of the individual scans shows a lower-envelope at about 10 mJy $\sqrt{\text{sec}}$ which does not change with 225 GHz zenith opacity between 0.07 and 0.5, and between elevations of 20 to 60°. At higher elevations, the lower envelope of the NEFD values increases somewhat. The median NEFD is 13 mJy $\sqrt{\text{sec}}$ with the standard pipeline used for the quick view. 63% of scans have a number of healthy channels>90 at Tau<0.2.

We also analyzed the two data sets of the Galactic Center and of NGC 604 in M 33 in more detail, using different filtering options of `crush`. Processing optimized to retrieve faint and extended emission, results in NEFDs of 10 mJy $\sqrt{\text{sec}}$ and better. The noise in the resulting maps (rms in MJy/sr) is about constant for the `crush` filtering options *deep* or *faint-extended*, but increases by a factor 4-5 when using the *extended* option, which is appropriate for extended but strong sources.

We also studied the observing efficiency of five of the observed projects by comparing the total observing time including telescope overheads due to calibration, pointing, focussing, slewing, with the on-source time. Typical overheads for single science targets on the sky are ~60%. However, they increase to 160% for a project where fairly bright point-like source were distributed all over the sky, and hence slewing times dominated.

The relative flux stability is about 8%, as derived from the scatter of five of the pointing sources with fluxes between 80 mJy and 23 Jy used during the run.

## 1 Overhead estimates

The overhead was estimated for 5 projects, considering calibration, focus, pointing and slewing time. GISMO observations typically comprise 5 minutes of pointing (including slewing time) every hour of science, 5 minutes of calibration every hour of science and 15 minutes of focusing every two hours of science. For single science sources, a typical value of ~60% was found. In case a project has target sources spread all over the sky, like 233-11, overheads are much larger, i.e. 160%. Results are summarised in Tab. 1. In the following some statistic about the bolometer is presented.

Table 1: Estimated overheads relative to on-source time.

| Project | Tot. time (h) | Overhead | Notes |
|---|---|---|---|
| 209-11 | 6.1 | 63% | NGC604/M33, Quintana-Lacaci, Kramer |
| 233-11 | 7.9 | 160% | AGNs, Edge |
| 247-11 | 15.1 | 60% | COSMOS deep field, Karim & Staguhn |
| 250-11 | 20.5 | 61% | GISMO deep field, Staguhn |
| 251-11 | 6.6 | 50% | Abell 1703, Schaerer |

## 2 Sensitivity

A total of 935 scans with measured NEFD were considered for the sensitivity estimate, from the April 2012 pool. We reduced these scans without applying filtering options, but with a pipeline analogous to that used during the pool, and extracting the NEFDs from the resulting logbook. In Fig 1, NEFD *vs* the 225 GHz zenith opacity, Tau, measured by a taumeter, is plotted, only for scans taken with at least 100 healthy channels (362 scans, 39% of the total). An additional axis (color gradient) represents the Elevation. The median value is 13 $mJy \cdot \sqrt{sec}$, with a mean and RMS of 15 $mJy \cdot \sqrt{sec}$ and 6, respectively. No trend with Tau is visible from the plot.

In Fig. 2, NEFD *vs* Elevation is plotted, applying the same threshold. Also in this case no trend with Elevation is visible, and thus no trend due to atmosphere.

In Fig. 3, a plot for NEFD *vs* number of healthy channels is presented. A mild dependence can be seen, in particular the spread of NEFD reduces above 100 channels, improving the sensitivity.

In Fig. 4 and 5 the number of healthy channels *vs* Tau at 225 GHz and elevation is plotted. No dependence from elevation can be seen, while most of scans (63%) with more than 90 healthy channels have been taken with Tau<0.2.

## 3 Flux-density stability

In Figs. 6, 7, 8, 9 and 10 the integrated flux-densities *vs* Tau for frequently observed pointing sources are plotted, namely: Mars, Neptune, 0133+476, 0316+413 and 0923+39. These plots allow one to verify the stability of flux-density measurements. The mean is plotted as solid line, while ±1 RMS levels are in dashed lines. A typical relative uncertainty of ~8% was found. Mean, RMS, and RMS as percentage of the mean flux-density for the sources considered here are presented in Tab. 2. The scans relative to these sources were reduced with the *-bright* option, using the integrated flux produced from the pipeline, and imposing a threshold of 90 healthy channels.

The Neptune scans taken during April 11th (from #30 to #40) were used to calculate the Jy/counts conversion factor, assuming a flux-density for Neptune of 6.2 Jy (`astro/gildas`). Mean and RMS are 5.59 Jy and 0.20, respectively. Mars flux-density from `astro/gildas` is 334 Jy, within the RMS found during the pool for flux-density measurements of this planet, thus confirming the accuracy of the conversion factor.

Table 2: Statistic for the 5 pointing sources considered here: mean flux-density, RMS (both in Jy) and RMS as percentage of the mean flux-density.

| Source | Mean | RMS | RMS% |
|---|---|---|---|
| Mars | 316 | 23 | 7% |
| Neptune | 5.58 | 0.39 | 7% |
| 0133+476 | 1.31 | 0.08 | 6% |
| 0316+413 | 11.7 | 0.8 | 7% |
| 0923+392 | 3.82 | 0.49 | 13% |

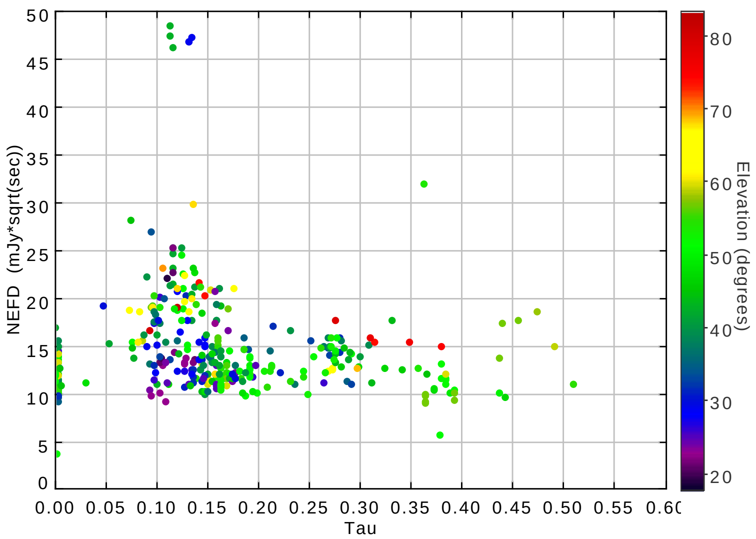


Figure 1: NEFD *vs* Tau at 225 GHz, applying the threshold of 100 healthy channels. The third axis (color gradient) represents the elevation of the scans.

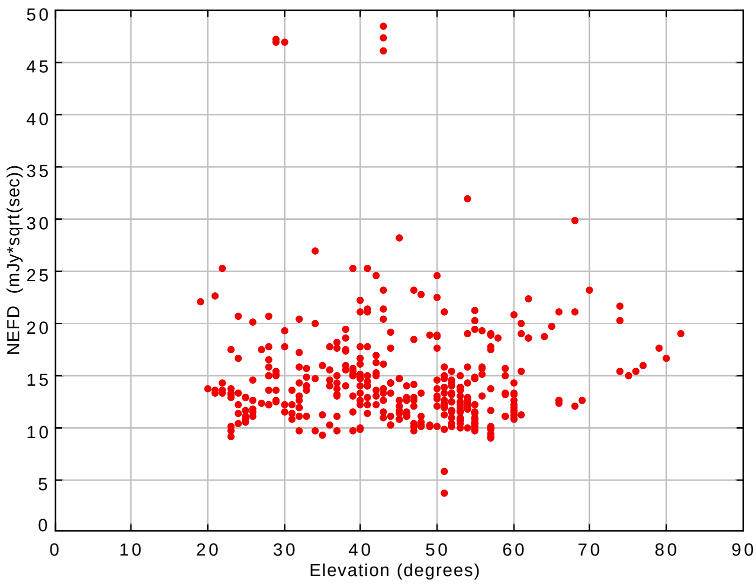


Figure 2: NEFD *vs* Elevation, applying the threshold of 100 healthy channels.

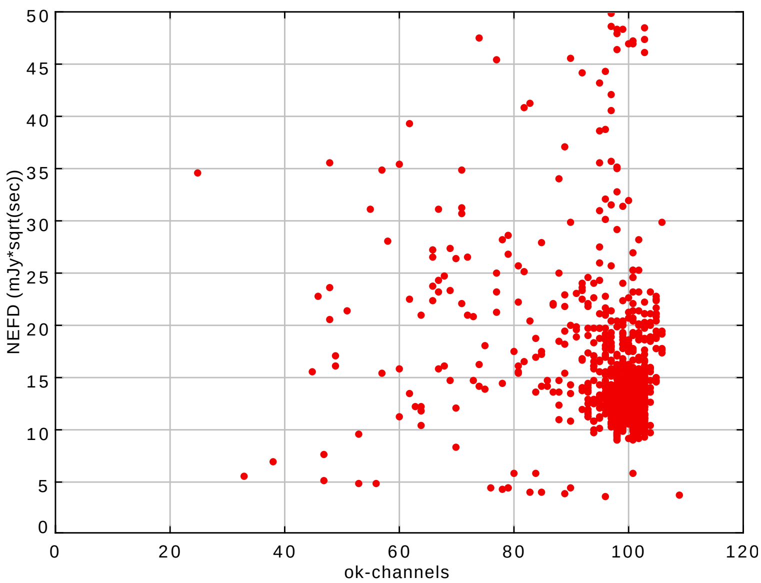


Figure 3: NEFD *vs* number of healthy channels in the GISMO array.

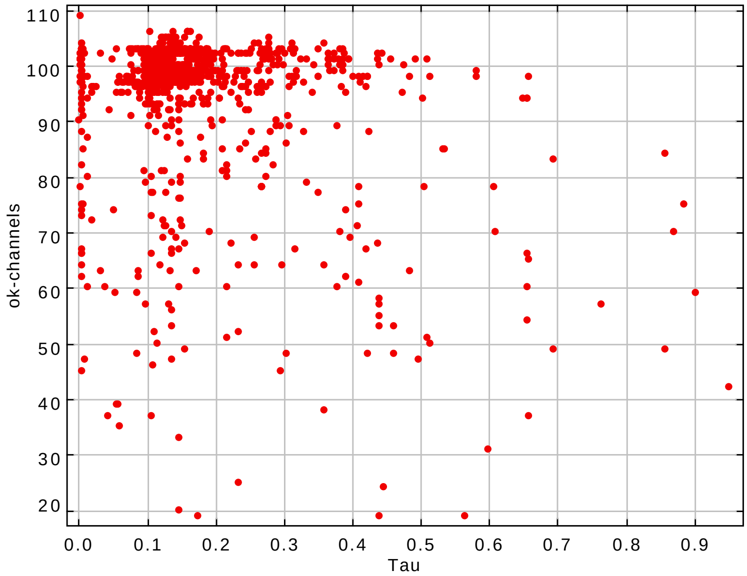


Figure 4: Number of healthy channels *vs* Tau at 225 GHz.

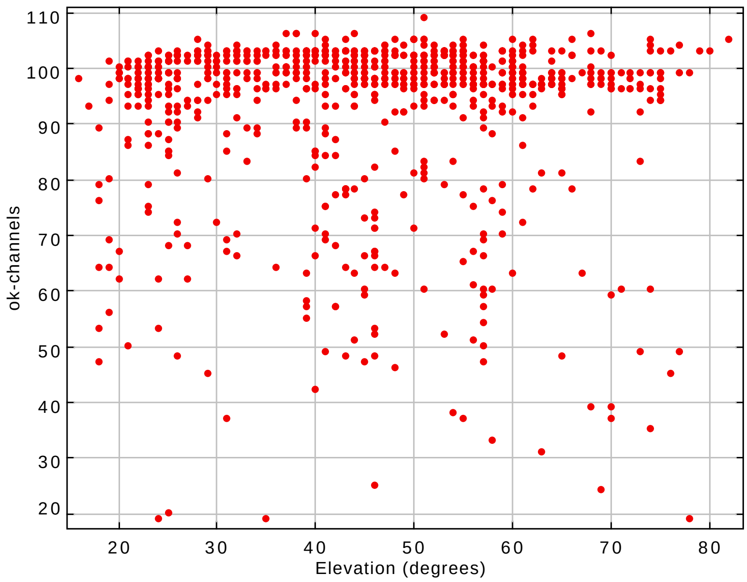


Figure 5: Number of healthy channels *vs* elevation.

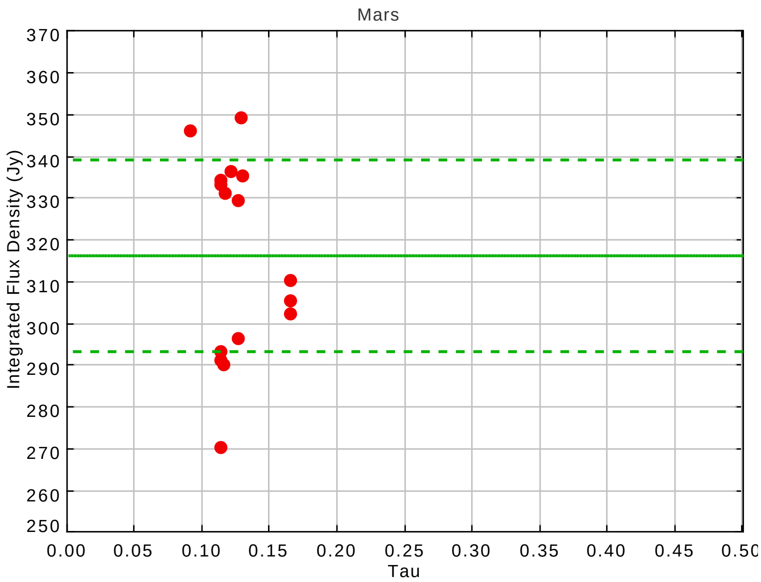


Figure 6: Mars integrated flux-densities *vs* Tau

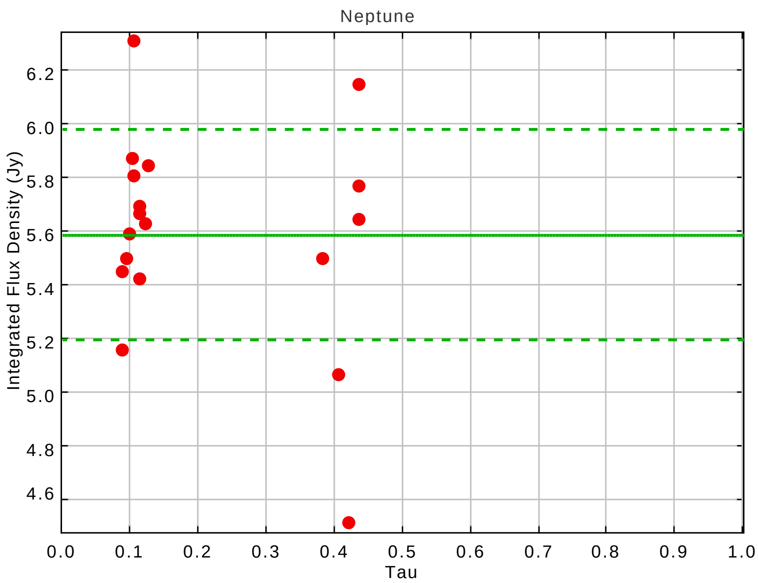


Figure 7: Neptune integrated flux-density *vs* Tau.

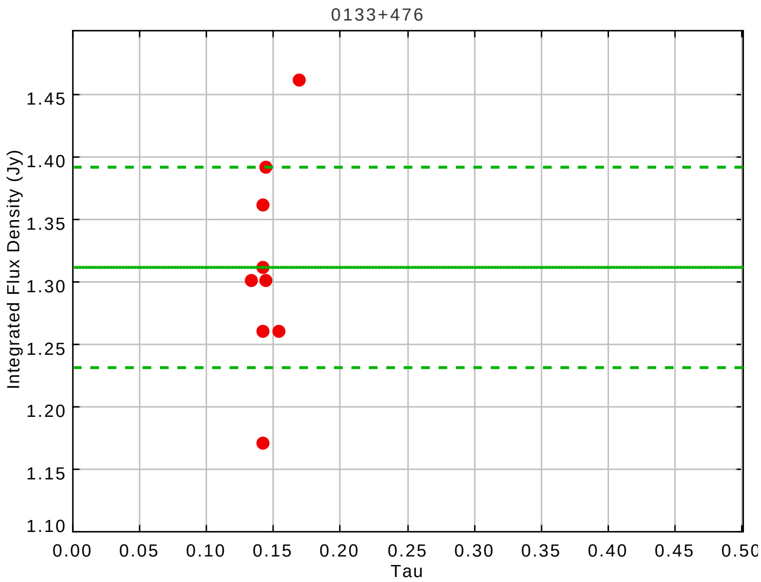


Figure 8: 0133+476 integrated flux-density *vs* Tau.

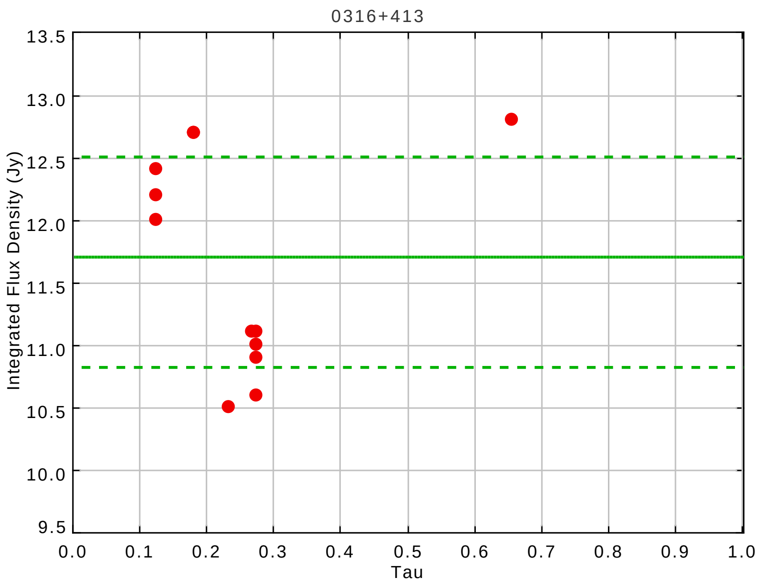


Figure 9: 0316+413 integrated flux-density *vs* Tau.

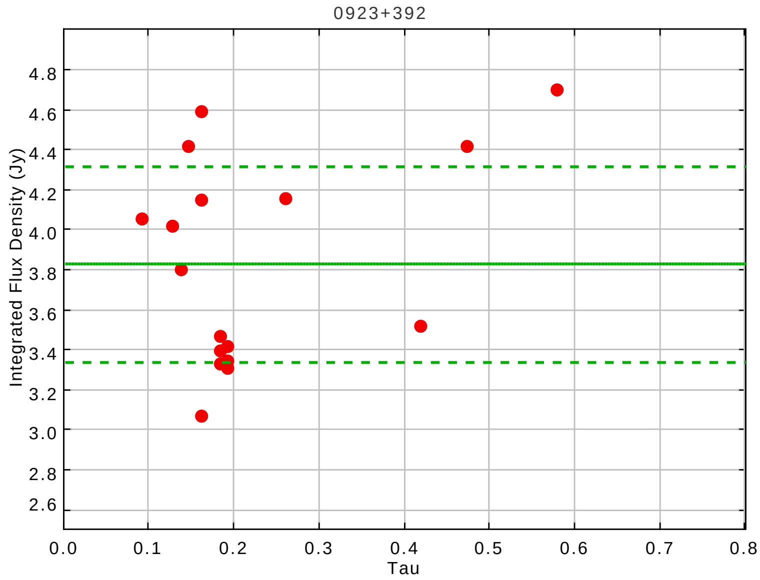


Figure 10: 0923+392 integrated flux-density *vs* Tau.

# 4 Image processing with CRUSH

In the following, the data reduction of two science targets from the first pool, using the CRUSH 2.12-1 suite, is shown. The final image for the NGC 604 HII region in M33 (project 209-11) is presented in Fig. 11. The section and image of NGC 604 have been extracted from Kramer et al. 2012. Figures 12 and 13 show the RMS resulting from the different reducing options, for the two sources, normalized to the value obtained with the *deep* option (the most aggressive one).

## 4.1 NGC 604

Observations of NGC 604 were conducted on April 21 to 23, 2012 (Kramer et al. 2012), during 6.2 hours of total observing time by repeated, fast on-the-fly scanning maps in perpendicular directions of 10’ × 10’ in size. Typical scanning speeds were 44”/s. Scanning directions alterated between Azimuth and Elevation. To check the pointing, about every hour a small Lissajous map of one minute was done on the nearby quasar 0133+476. Pointing corrections were applied by interpolating between successive pointings using the data reduction package crush (Kovács 2008). As the pointing source was always detected well inside the filled array, data reduction a posteriori is sufficient. The final pointing accuracy is ∼ 2”. Focus measurements were done by pointings at five different focus positions, and corrected online. The observing over- heads for pointing, focussing, and slewing are ∼ 60%.

To correct for atmospheric transmission, the opacities measured by the IRAM taumeter were used which measures the sky opacity at 225GHz scanning the sky in elevation (sky- dips) about every 4 minutes at a fixed position in azimuth. To obtain the positions of the GISMO pixels on the sky and source gains, Mars was mapped covering the source with each pixel.

Table 3: Total flux density of NGC 604, peak flux density, and rms, for different filter schemes of the reduction pipeline (Kramer et al. 2012). The ratio between the RMS for the various options and the *deep* option is given in columns 6 and 7. The last column reports the median NEFD.

| Filtering options[a] | Total (mJy) | Peak (mJy/beam) | rms[b] (mJy/beam) | rms (MJy/sr) | ratio (mJy/beam) | ratio (MJy/sr) | beam[c] ($''$) | NEFD (mJy$\cdot\sqrt{sec}$) |
|---|---|---|---|---|---|---|---|---|
| deep | 9.18 | 9.8 | 0.50 | $5.8\,10^{-3}$ | - | - | 24.75 | - |
| faint | 42.8 | 13.7 | 0.71 | $8.3\,10^{-3}$ | 1.4 | 1.4 | 21.03 | - |
| faint, ext., 25 | 58.5 | 13.4 | 0.68 | $8.0\,10^{-3}$ | 1.4 | 1.4 | 21.03 | 6.9 |
| faint, ext., 50 | 58.5 | 14.2 | 0.68 | $8.0\,10^{-3}$ | 1.4 | 1.4 | 21.03 | - |

**Notes:** *a*: We used `crush` version 2.12-b1 (beta). The number is the number of iterations. The default is 20. *b*: the rms is measured in a $1'$ aperture at 01:34:22.435 30:45:32.78. *c*: Effective resolution after convolving the data at the resolution of the telescope half power beam width (HPBW) with a Gaussian.

Figure 11 shows the resulting GISMO map of NGC 604, created with crush optimizing the result for faint and extended emission. We checked the robustness of the measured total flux density of NGC 604 by varying different filter schemes in the data processing pipeline (Tab. 3). The median NEFD obtained with the *faint-ext-25* option is 6.9 $mJy\cdot\sqrt{sec}$. Applying aggressive filtering "deep" to the time line of the data, subtracting the common mode assuming it is coming from the atmosphere or the instrument, is appropriate for point sources and deep fields. Here, however, it leads to a significant reduction of integrated flux densities while a softer filtering appropriate for faint (S/N<10 in single scans), extended sources leads to stable results. NGC 604 is detected with a signal-to-noise ratio of more than 20, a peak flux density of 13 mJy/beam, and a total flux density of 54 mJy. The rms of the inner, best sampled part of the map is $\sigma \sim 0.6$ mJy/beam.

## 4.2 The Galactic Center

Observations of the Galactic Center have been carried out from April 11th to 22nd, 2012 (project 190-11, PI: Staguhn J.). The tau varied from 0.1 to 0.3. Similar observation criteria used for NGC 604 were applied. Various reduction of the dataset were performed, selecting different options and round numbers. An on-source and an off-source regions were selected to estimate the typical RMS and the flux-density of SgrA*. Results are presented in Tab. 4, together with the applied reduction options, beam, RMS and peak flux-density. In the last column the median NEFD for the various reduction options is given. The value obtained applying the standard pipeline (no options) was 11.1 $mJy\cdot\sqrt{sec}$.

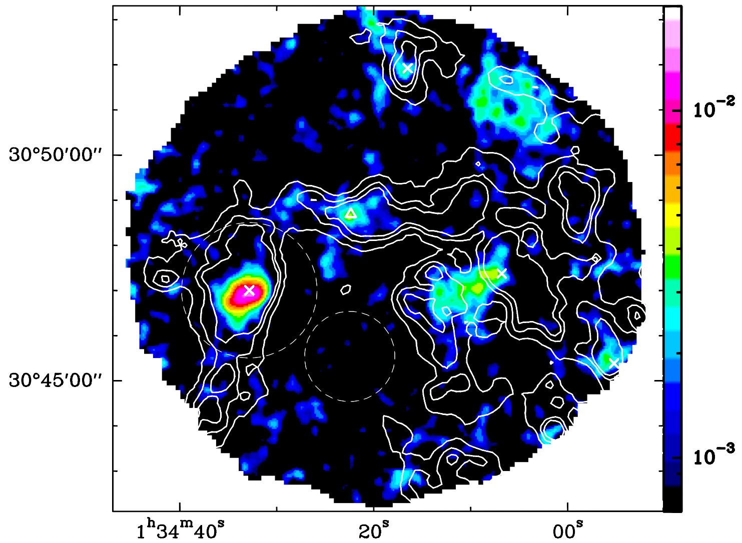


Figure 11: GISMO 2 mm map of the northern inner arm of M33 covering about 10'×10', from Kramer et al. 2012. Units are Jy/beam. Contours of 250 $\mu$m SPIRE emission are overlayed (Xilouris et al. 2012). From east-to-west, the map covers the $H_{II}$ regions NGC 604, BCLMP 691, BCLMP 302, and IC 142 which are marked by crosses. A dashed circle centered on NGC 604, marks the 3' aperture for photometry. The smaller dashed circle marks an area devoid of emission where the rms was measured (Tab. 3 ).

Table 4: Integrate flux density for SgrA* (from the Galactic Center map), peak flux density of the map, and rms for different filter schemes of the reduction pipeline. Also the ratio between the RMS for the various options and the *deep* option is given. The last column reports the median NEFD for the various options.

| Filtering options | SgrA* (Jy) | Peak (mJy/beam) | rms (mJy/beam) | rms (MJy/sr) | ratio (mJy/beam) | ratio (MJy/sr) | beam ($''$) | NEFD (mJy$\cdot\sqrt{sec}$) |
|---|---|---|---|---|---|---|---|---|
| no options | - | - | - | - | - | - | - | 11.1 |
| deep | 2.1 | 1.4 | 1.5 | $0.02\,10^{-3}$ | - | - | 24.75 | 9.4 |
| faint, ext., 25 | 28.0 | 14.8 | 2.7 | $0.03\,10^{-3}$ | 1.8 | 1.5 | 21.03 | 8.8 |
| faint, ext., 50 | 3.6 | 10.4 | 2.5 | $0.03\,10^{-3}$ | 1.7 | 1.5 | 21.03 | 9.6 |
| extended, 25 | 34.2 | 13.8 | 9.9 | $0.08\,10^{-3}$ | 6.6 | 4 | 17.73 | 7.8 |
| extended, 50 | 40.0 | 15.2 | 11.5 | $0.10\,10^{-3}$ | 7.7 | 5 | 17.73 | 8.1 |

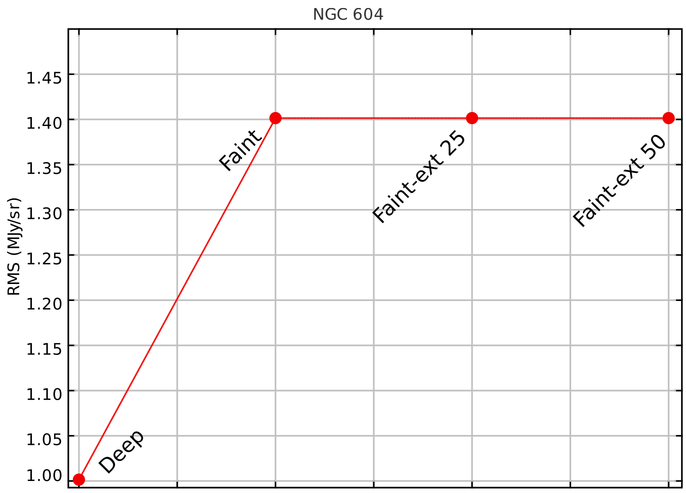


Figure 12: RMS (MJy/sr) of NGC 604 for the different reducing options, normalized to the RMS obtained with the *deep* option.

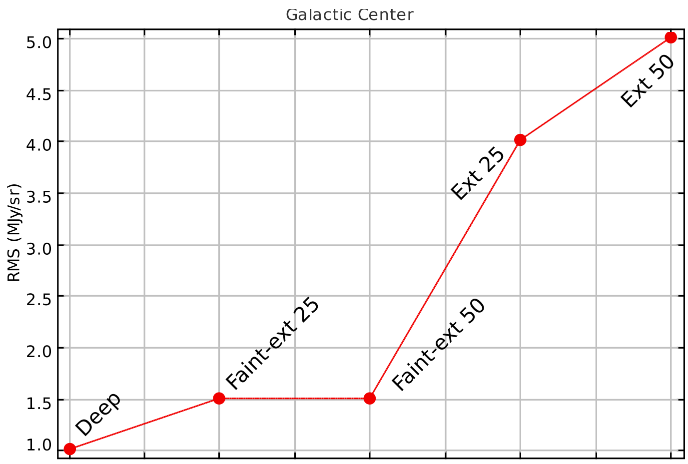


Figure 13: RMS (MJy/sr) of the Galactic Center for the different reducing options, normalized to the RMS obtained with the *deep* option.

## References

Kramer C., Quintana-Lacaci G., Israel F. et al. 2012, A&A (in prep.)
Staguhn J., Kovács A., Walter F. et al. 2012, AAS Meeting 220, 308.01